# ZVS-Enhanced and RMS-Current-Minimized Optimal Modulation Scheme of Dual-Active Bridge Converter With Comprehensive ZVS Analysis

Gayoung Park, *Graduate Student Member, IEEE*, Hwigon Kim, *Member, IEEE*, Byung-Geuk Cho, and Shenghui Cui, *Member, IEEE*

***Abstract*—In applications of the dual-active bridge (DAB) converters, minimizing circulating current and maximizing zero-voltage switching (ZVS) capability are crucial to ensure high efficiency and reliable operation. To address these challenges, this article proposes an optimal triple-phase-shift modulation scheme for the DAB converter. The proposed scheme minimizes rms current and achieves ZVS with minimal increase in circulating current across the entire load range. Building on previous modulation strategies, this article introduces a comprehensive ZVS analysis. It establishes precise ZVS criteria by rigorously accounting for the nonlinear voltage characteristics of parasitic MOSFET capacitances and the dynamic circuit behavior during the dead time, factors often simplified or overlooked in prior approaches. Using nonlinear optimization constrained by these precise ZVS criteria, the proposed modulation scheme guarantees a wide ZVS range without requiring excessive circulating current for complete ZVS, significantly reducing both switching and conduction losses. For experimental validation, a 20 kW/50 kHz SiC-based DAB converter was built, where the converter achieved a peak efficiency of 98.8%, thereby confirming the effectiveness of the proposed method.**

***Index Terms*—Dual-active bridge (DAB), dynamic circuit behavior, triple-phase-shift (TPS), zero-voltage switching (ZVS).**

## I. Introduction

DUAL-ACTIVE bridge (DAB) is a dc–dc converter topology utilized in high-power applications [1], known for its bidirectional power transfer capability and galvanic isolation. With its wide voltage conversion range and flexibility in power flow direction, the DAB offers significant advantages in applications where high efficiency and high power density is crucial, such as electric vehicle (EV) charging, interfacing with energy storage systems, and dc distribution systems.

The operation and resulting efficiency of the DAB are closely related to the modulation strategy. From single-phase-shift (SPS) modulation, which simply adjusts the phase-shift angle between the two full bridges [2], [3], the control methods of the DAB have evolved to offer greater controllability. The dual-phase-shift (DPS) [4], [5] and extended-phase-shift [6], [7] modulation schemes both utilize two degrees of freedom (DOF), while triple-phase-shift (TPS) modulation employs three DOFs to control the phase-shift angle and the duties of both full-bridges [8]. Additional DOFs can be achieved by varying the frequency [9], [10] or adopting asymmetric modulation [11], although these approaches increase computational complexity and challenges in practical implementation. TPS modulations, in particular, have been extensively studied, with optimization of the three DOFs for various objectives to improve efficiency.

Efficiency can be primarily enhanced by overcoming large circulating current and loss of zero-voltage switching (ZVS) under unmatched voltage gain and light- to medium-load conditions [12]. Literature has explored TPS modulation schemes to minimize circulating current based on optimization [13], [14], [15], [16], [17], [18], [19], [20], [21], [22], [23], [24], [25], [26], [27], [28], [29], [30]. To reduce the circulating current, it is crucial to select an appropriate parameter indicating the amount of it, such as power loss [13], [14], reverse power [27], rms value of the inductor current [16], [17], [18], [19], [20], [21], [22], [23], current stress [24], [25], [26], [27], [28], and multiobjective optimization combining several metrics [30]. Optimal modulation parameters that minimize such objectives are derived either through analytic derivation using Lagrange multiplier method [13], [15], [18], [19], [20], [21], [23], [24], [25], [26], [27], [28] or through numerical optimization [14], [16], [17], [22], [30]. Among these optimization targets, the inductor rms current is directly related to conduction loss, which constitutes a significant portion of the total loss [23]. However, optimizing rms current leads to a complicated, nonconvex optimization problem, whereas using peak current stress as the objective simplifies both calculation and optimization [25]. To effectively address this challenge, this article adopts a numerical optimization approach, ensuring greater accuracy and practicality in rms current optimization.

Received 22 September 2024; revised 5 January 2025; accepted 3 February 2025. Date of publication 13 February 2025; date of current version 14 April 2025. This work was supported in part by LG Innotek Company Ltd. and in part by the Korea Institute of Energy Technology Evaluation and Planning (KETEP) grant funded by Korea Government (MOTIE) under Grant 20224000000160 (DC Grid Energy Innovation Research Center). Recommended for publication by Associate Editor J. Biela. *(Corresponding author: Shenghui Cui.)*

Gayoung Park, Hwigon Kim, and Shenghui Cui are with the Department of Electrical and Computer Engineering and SNU Electric Power Research Institute, Seoul National University, Seoul 08826, South Korea (e-mail: rabbithood2580@snu.ac.kr; whguswn6994@snu.ac.kr; cuish@snu.ac.kr).

Byung-Geuk Cho is with the LG Innotek Company Ltd., Seoul 07796, South Korea (e-mail: bkei80@lginnotek.com).

Color versions of one or more figures in this article are available at https://doi.org/10.1109/TPEL.2025.3541847.

Digital Object Identifier 10.1109/TPEL.2025.3541847

Based on the loss analysis presented in [15], switching losses contribute significantly to the overall losses, particularly under light-load conditions, in addition to conduction losses. Although zero-current switching (ZCS) can be achieved with rms-current-minimized approaches [15], [16], [17], [22], achieving ZVS is preferred over ZCS for MOSFET-based switching converters due to the considerable stored energy that results from parasitic capacitances [31]. Furthermore, smoothed voltage waveforms under accomplishment of the ZVS can suppress high-frequency crosstalk and electromagnetic compatibility issues [21]. Consequently, numerous studies have incorporated ZVS constraints into the optimization process of TPS modulation to expand the ZVS range of the DAB [14], [18], [19], [20], [21], [23], [24], [25], [26], [28], [29], [30].

Achieving ZVS in switches comes at the cost of increased circulating current. Therefore, it is crucial to minimize the turn-OFF current required to discharge the MOSFET parasitic capacitance and realize complete ZVS, commonly referred to as "ZVS-current" [21]. In this article, techniques for calculating ZVS-current and establishing the ZVS boundary are revisited through a detailed review of previous works. The simplest method for determining the ZVS boundary considers only the direction of the turn-OFF current [26], [28], which neglects the influence of parasitic capacitances. Determining the ZVS-current solely based on inductive energy or capacitive charge [18], [19], [20], [24], [30] may still yield inaccurate results. To refine the ZVS boundary calculations, the effects of the secondary-side circuitry are incorporated in [10] and [14]. However, these studies omit the impact of dead time, which, if too short, can prevent complete ZVS, or if too long, can cause re-resonance. Dead-time control, proposed in [25], addresses this issue by factoring in the effect of dead time to achieve ZVS. Although it eliminates unnecessary circulating current during antiparallel diode commutation, the complexity of dead-time control poses challenges for practical implementation. Recent works [11], [21], [23], [32] further investigate current commutation during the dead time. However, these studies overlook the time-dependent dynamic behavior of the circuit during dead time, such as the nonlinear drain-source voltage dependence of MOSFET parasitic capacitances. By simplifying circuit operation during this period, these approaches introduce excessive margins in optimizing ZVS-current, limiting the accuracy of ZVS constraints and expansion of the ZVS region.

To address the lack of comprehensive analysis in establishing an accurate ZVS boundary for enhanced efficiency, this article introduces an optimal TPS modulation scheme combined with an in-depth ZVS analysis for the practical realization of complete ZVS. The key contributions of this work are as follows.

1) This article presents a comprehensive quantitative analysis of dynamic circuit behavior during dead time. Accurate ZVS constraints are derived by considering dead time effects, MOSFET parasitic capacitances, and switch behavior across various operating conditions.
2) An optimal TPS modulation scheme is proposed to minimize rms current while ensuring ZVS. This approach reduces conduction and switching losses, expands the ZVS region across a wide range of loads and operating voltages, and improves overall efficiency.

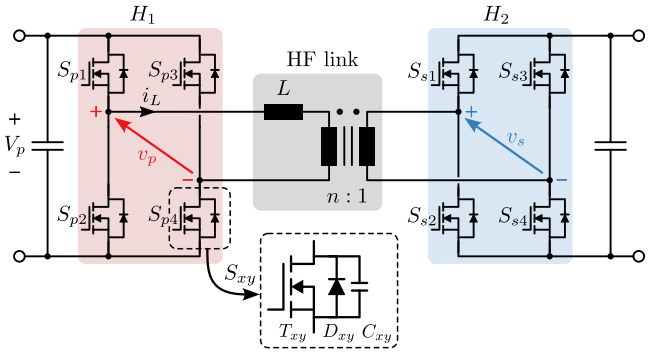


Fig. 1. Circuit diagram of the DAB converter.

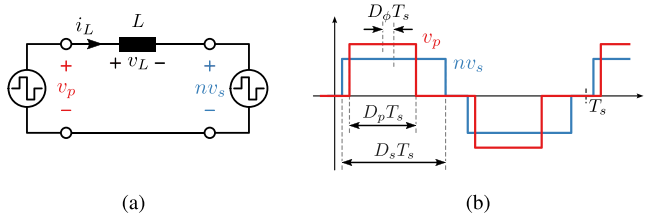


Fig. 2. (a) Equivalent circuit diagram of DAB. (b) AC voltage waveforms of $H_1$ and $H_2$ for the DAB under TPS modulation.

3) The proposed method is experimentally validated across a broad operating voltage range and up to a rated power of 20 kW. A detailed analysis of the results confirm its effectiveness and practical advantages.

The rest of this article is organized as follows. Section II describes the operating principles of the DAB converter under TPS modulation. Section III provides a detailed analysis of ZVS operation, establishing the requirements for achieving complete ZVS and introducing a piecewise approximation of inductor current during dead time for precise calculation of the ZVS-currents. Section IV presents the proposed TPS modulation scheme, which enhances ZVS and minimizes rms current. Section V experimentally validates the proposed method using a 20 kW DAB prototype, demonstrating its effectiveness across diverse operating conditions. Finally, Section VI concludes this article.

## II. Operating Principles of the DAB Converter With TPS Modulation

This section discusses the operation principles of the DAB converter under TPS modulation. The DAB consists of two full-bridge circuits connected via a high-frequency transformer, as illustrated in Fig. 1. The dc voltages on the primary and secondary sides are denoted as $V_p$ and $V_s$, respectively. The leakage inductance referred to the primary side and turns ratio of the transformer are denoted as $L$ and $n$. A simplified equivalent circuit of the DAB is shown in Fig. 2(a). In TPS modulation, as depicted in Fig. 2(b), the power transferred through the DAB is controlled by three variables: The duty cycles of both full-bridges, $D_p$ and $D_s$, and the phase-shift ratio between the two full bridges, $D_\phi$.

The rest of this section presents both time-domain and frequency-domain analyses, deriving useful expressions for the nonlinear optimization discussed in Section IV.

### A. Time-Domain Analysis of DAB Operation

Through time-domain analysis, the operating modes of the DAB converter are categorized based on their voltage and current waveforms [16], [33]. Building on the literature, this article introduces five operating modes with low circulating currents: Modes I, II, III, IV, and V. For each mode, the inductor current at switching instants and the relationships between modulation parameters are detailed in this section, forming the basis for defining the operating mode and ZVS constraints in the optimization problem discussed in Section IV. The operating waveform under each mode is illustrated in Fig. 3 for both buck- and boost-type operation. In this section, only buck-type powering operation is addressed, where $D_p \leq D_s$ and $D_\phi > 0$, without loss of generality.

In each mode, as in Fig. 3, the current at the switching of a switch $S_{xy}$ is denoted as either $-I_{xy}$ (primary) or $I_{xy}$ (secondary), with $I_{xy}$ defined to be positive when ZVS is achieved. Here, "$x$" can be either "$p$" (for primary) or "$s$" (for secondary), and "$y$" can be any of $\{1, 2, 3, 4\}$, as illustrated in Fig. 1. To be specific, $S_{p1}$ and $S_{p4}$ are turned ON at the positive and negative rising edges of $v_p$, respectively, while $S_{s1}$ and $S_{s4}$ are turned ON at the corresponding rising edges of $nv_s$.

As depicted in Fig. 3, the operating mode transitions from mode I to mode V as the output power increases, evolving from light-load to heavy-load operation. Three distinct operating regions are defined based on the number of switches achieving ZVS and the output power level as follows.

1) *Light-Load Operation:* In the light-load region, the DAB operates in modes I and II, achieving ZVS for all switches (referred to as "all-ZVS"). The switch currents, $I_{p1}$, $I_{p4}$, $I_{s1}$, and $I_{s4}$, can take positive values, as shown in Fig. 3(a)–(d). As power increases, $D_s$ reaches 0.5 as in Fig. 3(c), and the operating mode is switched from mode I to mode II.
2) *Medium-Load Operation:* In the medium-load region, the DAB operates in modes II and III, achieving ZVS for up to six switches (referred to as "six-ZVS"). While mode II ensures all-ZVS under light-load operation, this becomes infeasible as the load increases. A detailed analysis of the ZVS capabilities in modes II is provided in Section IV.
   As the load further increases as in Fig. 3(e), the operating mode shifts to mode III when the positive rising edges of $v_p$ and $nv_s$ coincide as $D_\phi$ increases. Since $-I_{p1}$, $I_{s1}$, and $I_{s4}$ are equal, the operation with mode III leads to the loss of ZVS capability for the corresponding switches. Therefore, all-ZVS is intrinsically impossible to achieve with mode III operation. Either six switches can fulfill ZVS if $I_{p1}$ is negative, or four switches can fulfill ZVS (referred to as "four-ZVS") if $I_{s1}$ and $I_{s4}$ are negative. Fig. 3(e) and (f) show the six-ZVS case, which is adopted for the proposed modulation scheme.

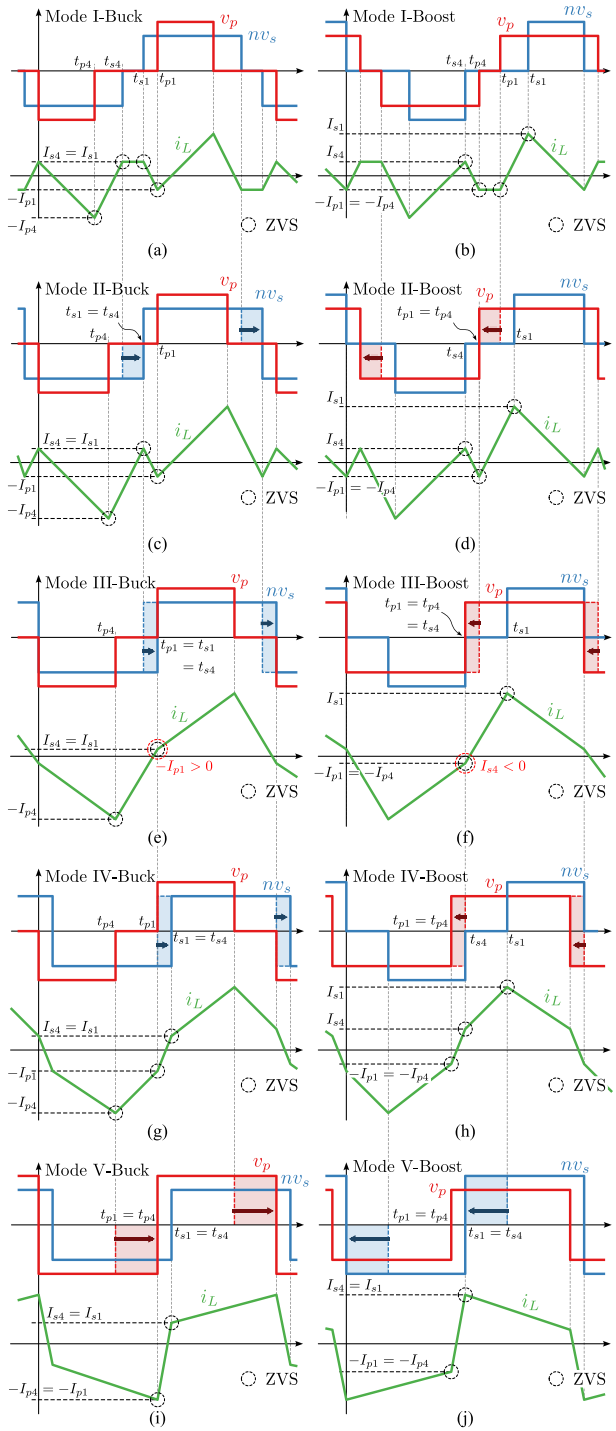


Fig. 3. Operating waveforms of ac voltages and inductor current under buck-type and boost-type operation modes. (a) Mode I-Buck. (b) Mode I-Boost. (c) Mode II-Buck. (d) Mode II-Boost. (e) Mode III-Buck. (f) Mode III-Boost. (g) Mode IV-Buck. (h) Mode IV-Boost. (i) Mode V-Buck. (j) Mode V-Boost.

3) *Heavy-Load Operation:* In the heavy-load region, the DAB operates in modes IV and V, where all-ZVS is achievable as power increases, as illustrated in Fig. 3(g)–(j). When the positive rising edge of $v_p$ leads that of $nv_s$ as $D_\phi$ increases as in Fig. 3(g), the operation is altered from

TABLE I
CATEGORIZATION OF STEADY-STATE OPERATING MODES AND EXPRESSIONS OF INDUCTOR CURRENTS

| Categorization | | Mode I | Mode II | Mode III | Mode IV | Mode V |
|---|---|---|---|---|---|---|
| Buck-Type | Mode Constraints | $D_s - D_p < 2D_\phi$ | | $D_s - D_p = 2D_\phi$ | $D_p + D_s > 1 - 2D_\phi$ | |
| | | $D_p < D_s < 0.5$ | | $D_p < D_s = 0.5$ | | $D_p = D_s = 0.5$ |
| | Normalized Currents | $i_{p1} = (1-M)D_p - 2MD_\phi$<br>$i_{p4} = (1-M)D_p + 2MD_\phi$<br>$i_{s1} = -D_p + MD_s$<br>$i_{s4} = -D_p + MD_s$ | | $i_{p1} = (1+M)D_p + 2MD_\phi - M$<br>$i_{p4} = (1-M)D_p + 2MD_\phi$<br>$i_{s1} = (-1+M)D_s + 2D_\phi$<br>$i_{s4} = (1+M)D_s + 2D_\phi - 1$ | | |
| Boost-Type | Mode Constraints | $D_p - D_s < 2D_\phi$ | | $D_p - D_s = 2D_\phi$ | $D_p + D_s > 1 - 2D_\phi$ | |
| | | $0.5 > D_p > D_s$ | | $D_p = 0.5 > D_s$ | | $D_p = D_s = 0.5$ |
| | Normalized Currents | $i_{p1} = D_p - MD_s$<br>$i_{p4} = D_p - MD_s$<br>$i_{s1} = (M-1)D_s + 2D_\phi$<br>$i_{s4} = (M-1)D_s - 2D_\phi$ | | $i_{p1} = (1+M)D_p + 2MD_\phi - M$<br>$i_{p4} = (1-M)D_p + 2MD_\phi$<br>$i_{s1} = (-1+M)D_s + 2D_\phi$<br>$i_{s4} = (1+M)D_s + 2D_\phi - 1$ | | |

modes III to IV. As depicted in Fig. 3(i), $D_p$ increases until it reaches 0.5 and the DAB starts to operate in mode V, which is in fact referred to as SPS modulation in literature.

The constraints for each mode and the inductor currents normalized to $\frac{V_p}{2f_sL}$ are summarized in Table I for both buck- and boost-type operations, where $M$ denotes the voltage ratio, $nV_s/V_p$, and $f_s$ refers to the switching frequency. A detailed discussion of practical ZVS capability in each operating region is provided in Section IV, based on the derived mode constraints and inductor currents.

### B. Frequency-Domain Analysis of DAB Operation

To formulate a nonlinear optimization problem for minimizing rms current, frequency-domain analysis is employed to derive expressions for rms current and power. These frequency-domain equations are presented in simplified forms, offering greater consistency compared to the time-domain expressions, which vary across operating modes. This simplification facilitates the nonlinear optimization process.

In the frequency domain, the voltage and current phasors of the DAB are expressed as the sum of harmonic components. The $h$th harmonic components of the ac voltage and current are expressed as follows:

$$\vec{V}_{p,h} = \frac{4V_p}{h\pi}\sin(D_p h\pi)\sin(0.5h\pi) \tag{1}$$

$$\vec{V}_{s,h} = \frac{4MV_p}{h\pi}\sin(D_s h\pi)\sin(0.5h\pi)e^{-jD_\phi h2\pi} \tag{2}$$

$$\vec{I}_{L,h} = \frac{\vec{V}_{p,h} - \vec{V}_{s,h}}{j2\pi h f_s L} = \frac{2V_p\sin(0.5h\pi)}{L(h\pi)^2 f_s j}\left[\sin(D_p h\pi) - M\sin(D_s h\pi)e^{-jD_\phi h2\pi}\right] \tag{3}$$

where all expressions of the voltage and current phasors are referred to the primary side, as shown in Fig. 2(a).

The total rms value of the current is calculated as follows:

$$I_{L,\mathrm{rms}}^2 = \sum_{h=1,3,\cdots}^{\infty} \left|\vec{I}_{L,h}\right|^2/2. \tag{4}$$

The $h$th harmonic active power is calculated using (1) and (3) as follows:

$$P_h = \frac{\mathrm{Re}(\vec{V}_{p,h}\cdot\vec{I}_{L,h})}{2} = \frac{4MV_p^2\sin(D_p h\pi)\sin(D_s h\pi)\sin(D_\phi h2\pi)}{L(h\pi)^3 f_s}. \tag{5}$$

The power and rms current of the DAB can be approximated using harmonic component analysis for simplicity of the expressions. For accurate approximation, harmonic components of current and transferred power are calculated considering up to the 3rd and 5th harmonics, respectively [22], as follows:

$$I_{L,\mathrm{rms}}^2 \cong \sum_{h=1,3}\frac{\left|\vec{I}_{L,h}\right|^2}{2} = \frac{\left|\vec{I}_{L,1}\right|^2 + \left|\vec{I}_{L,3}\right|^2}{2} \tag{6}$$

$$P_o \cong \sum_{h=1,3,5} P_h = P_1 + P_3 + P_5. \tag{7}$$

## III. COMPREHENSIVE ZVS ANALYSIS FOR WIDE ZVS RANGE

This section presents a comprehensive analysis of ZVS operation, deriving accurate ZVS-current requirements using a proposed approximation of inductor current. As discussed in the previous section, achieving all-ZVS across the entire load range of the DAB is infeasible. To extend the ZVS region and minimize the required inductor current, it is essential to establish precise criteria for the ZVS capability of the switches. Hence, it is crucial to determine accurate ZVS-current, the minimum current required at turn-OFF to fulfill complete ZVS operation.

The section begins by examining the dynamic circuit behavior during dead time, assuming no voltage drop across the antiparallel diodes. Given that the magnetizing inductance of the transformer, denoted as $L_m$, is typically much larger than the leakage inductance, its effect is considered negligible. The conditions necessary for ZVS are then identified. By comprehensively integrating these requisites into the analysis, the ZVS-current is computed using the proposed approximation, enabling a more precise and practical assessment of ZVS feasibility.

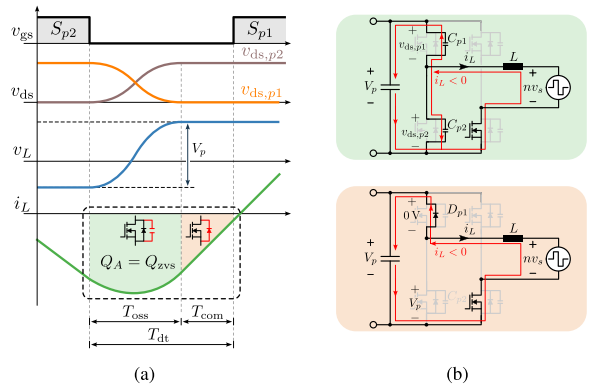


Fig. 4. Dynamic behavior of the DAB circuit during the dead time. (a) Transient voltages and current throughout the dead time. (b) Resonance between leakage inductance and MOSFET parasitic capacitances (top inset), followed by diode commutation after resonance (bottom inset).

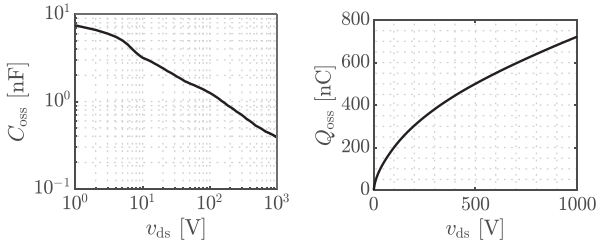


Fig. 5. (a) Parasitic output capacitance $C_{\rm oss}(v_{\rm ds})$ and (b) charge $Q_{\rm oss}(v_{\rm ds})$ of SiC MOSFET IMZA120R007M1H used in the investigated 20 kW DAB converter.

### A. Analysis of Dynamic Circuit Behavior During Dead Time

Without loss of generality, the dynamic behavior of inductor current is demonstrated investigating the leading leg on the primary side ($S_{p1}$, $S_{p2}$) under buck-type mode I operation, as illustrated in Fig. 4. As shown in Fig. 4(a), the other switching legs are assumed to maintain their initial state throughout the dead time. The antiparallel diode of a MOSFET switch $S_{xy}$ is denoted as $D_{xy}$, while its parasitic capacitance is represented as $C_{xy}$, as depicted in Fig. 1. Here, $C_{xy}$ varies as a nonlinear function of the drain-source voltage $v_{\rm ds}$, as shown in Fig. 5(a). The charge stored in $C_{xy}$, denoted as $Q_{xy}$, represents the stored charge $Q_{\rm oss}$, which is an integral of $C_{\rm oss}$ with respect to $v_{\rm ds}$, as shown in Fig. 5(b).

The detailed ZVS process is outlined as follows.

1) *Turn-off of $S_{p2}$:* Gate-source voltage of the lower switch decreases below the threshold voltage, turning OFF $S_{p2}$.
2) *Resonance between L, $C_{p1}$, and $C_{p2}$:* During resonance, the current charges $C_{p2}$ until $v_{{\rm ds},p2}$ reaches $V_p$, and discharges $C_{p1}$ until $v_{{\rm ds},p1}$ reaches 0 V, as depicted in the top inset of Fig. 4(b). The relations of the voltage and the current during resonance are stated as

$$V_p = v_{{\rm ds},p1} + v_{{\rm ds},p2} \tag{8}$$

$$i_L = C_{p1}(v_{{\rm ds},p1})\frac{dv_{{\rm ds},p1}}{dt} - C_{p2}(v_{{\rm ds},p2})\frac{dv_{{\rm ds},p2}}{dt} \tag{9}$$

where the direction of current is defined positive when $i_L$ is flowing towards the leakage inductance, as depicted in Fig. 4. Integrating (9) during the resonance yields

$$\int_{T_{\rm oss}} i_L dt = \int_{V_p}^{0} C_{\rm oss}(v_{\rm ds})dv_{\rm ds} - \int_{0}^{V_p} C_{\rm oss}(v_{\rm ds})dv_{\rm ds}$$
$$= -2\int_{0}^{V_p} C_{\rm oss}(v_{\rm ds})dv_{\rm ds} = -2Q_{\rm oss}(V_p) \tag{10}$$

where $T_{\rm oss}$ is the duration of the resonance. $Q_{\rm oss}(V_p)$ refers to the charge stored in $C_{p2}$ when $v_{{\rm ds},p2}$ has reached $V_p$. For ZVS-ON of $S_{p1}$, the resonance must complete within the dead time, $T_{\rm dt}$. In other words, integrated area of the inductor current is needs to reach $Q_{\rm zvs} = 2Q_{\rm oss}(V_p)$ before the dead time ends, as in Fig. 4(a).

3) *Current commutation through $D_{p1}$:* After resonance, the current begins flowing through the antiparallel diode $D_{p1}$, as shown in the bottom inset of Fig. 4(b). The duration of the body diode commutation phase is denoted as $T_{\rm com}$. During this process, the current direction may reverse, potentially leading to re-resonance and failure of complete ZVS [29].
4) *ZVS turn-on of $S_{p1}$:* At the end of the dead time, the gate-source voltage of the upper switch increases while $v_{{\rm ds},p1}$ remains at zero, thereby accomplishing the complete ZVS-on of $S_{p1}$.

### B. Considerations for Complete ZVS Operation

For the primary-side switch $S_{p1}$ to achieve complete ZVS at its switching instant $t_{p1}$, the following requisites must be satisfied simultaneously. These criteria apply to other switches as well.

1) *Direction of the current:* To initiate the ZVS process, the current at the beginning of the dead time should be negative as

$$i_L(0) \leq 0. \tag{11}$$

2) *Completion of resonance before dead time:* To fully charge and discharge $C_{\rm oss}$ of the switching leg, the resonance must complete within the dead time as

$$0 < T_{\rm oss} \leq T_{\rm dt}. \tag{12}$$

If the dead time is shorter than the resonance duration ($T_{\rm dt} < T_{\rm oss}$), $S_{p1}$ is forced to turn ON before $v_{{\rm ds},p1}$ reaches zero, resulting in incomplete ZVS (iZVS), as illustrated in Fig. 6(a).
3) *Prevention of re-resonance:* To avoid reversal of the resonance, the initial direction of the current should be conserved post-resonance as

$$i_L(T_{\rm dt}) \leq 0. \tag{13}$$

If the dead time is too long, the direction of the current is reversed before the dead time, charging and discharging $C_{p1}$ and $C_{p2}$ respectively. This re-resonance results in iZVS as well, as depicted in Fig. 6(b).

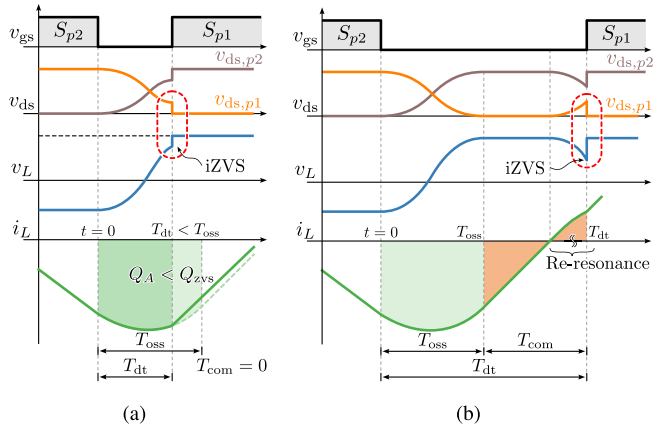


Fig. 6. Effect of dead time on ZVS operation. (a) Incomplete ZVS (iZVS) due to partial hard switching under short dead time. (b) iZVS due to re-resonance under long dead time.

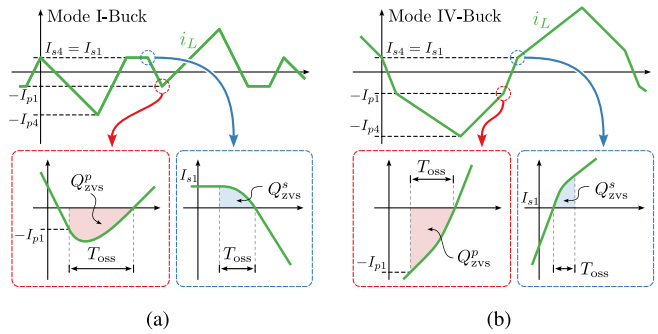


Fig. 7. Achieving complete ZVS and dynamic circuit behavior during the dead time under different operating conditions. (a) Buck-type mode I. (b) Buck-type mode IV.

4) *Dynamic circuit behavior during the dead time:* The circuit behavior during the turn-ON transient of each switch varies depending on the operating mode. Fig. 7(a) and (b) illustrate the inductor current during turn-ON transients of $S_{p1}$ and $S_{s1}$ under buck-type mode I and mode IV operations, respectively. The charge required for ZVS differs between the primary and secondary sides, denoted as $Q^p_{\rm zvs}$ and $Q^s_{\rm zvs}$, respectively.
In addition, as highlighted in the red-edged insets of Fig. 7, the required ZVS-current $I_{p1}$ varies depending on the distinct current waveform in each operating mode. Therefore, to ensure complete ZVS, the ZVS-current must be determined separately for each switch, considering its specific operating conditions and dynamic circuit behavior.

### C. Proposed Approximation of Dead-Time Inductor Current

In this section, a piecewise approximation of the dynamic inductor current during the dead time is proposed, as shown in Fig. 8. The current slope varies depending on the switching state and operating mode, which is expressed as

$$\frac{di_L}{dt} = \frac{v_p - nv_s}{L}. \tag{14}$$

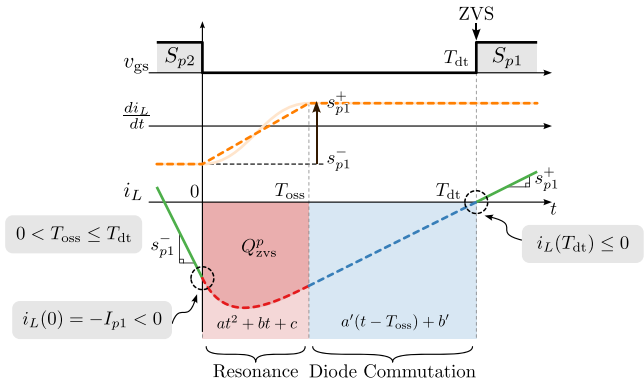


Fig. 8. Proposed approximation of dynamic current behavior during the dead time and requisites for complete ZVS.

TABLE II
SLOPES OF INDUCTOR CURRENT UNDER BUCK-TYPE MODE I OPERATION

| Edge | Switch | Slopes of Current | |
|---|---|---|---|
| | | $s^-_{xy}$ | $s^+_{xy}$ |
| Neg. rising edge of $v_p$ | $S_{p4}$ | $\frac{(-1+M)V_p}{L}$ | $\frac{MV_p}{L}$ |
| Pos. rising edge of $v_p$ | $S_{p1}$ | $\frac{-MV_p}{L}$ | $\frac{(1-M)V_p}{L}$ |
| Neg. rising edge of $nv_s$ | $S_{s4}$ | $\frac{MV_p}{L}$ | 0 |
| Pos. rising edge of $nv_s$ | $S_{s1}$ | 0 | $\frac{-MV_p}{L}$ |

As depicted in Fig. 8, during the turn-ON transient of $S_{p1}$, the current slope transitions from $s^-_{p1}$ to $s^+_{p1}$. Here, $s^-_{xy}$ and $s^+_{xy}$ denote the current slopes before and after the dead time for each switch $S_{xy}$, respectively. Table II summarizes the current slopes before and after the dead time for each switch, under buck-type mode I operation as an example.

During resonance, $v_{\rm ds}$ can be approximated to increase or decrease linearly with time, as in Fig. 8, considering the symmetry of the parasitic capacitances of the two complementary switches in the same leg. By integrating the linearly approximated inductor voltage, the inductor current $i_L$ is approximated as a quadratic function of the time during the resonance between $L$ and $C_{\rm oss}$ as follows:

$$i_L(t) = at^2 + bt + c \quad (0 \le t < T_{\rm oss}). \tag{15}$$

Substituting the initial condition of the inductor current, $i_L(0) = -I_{xy}$ (or $I_{xy}$ for the secondary side), and the boundary conditions for the slope of current, $i'_L(0+) = s^-_{xy}$ and $i'_L(T_{\rm oss}-) = s^+_{xy}$, the coefficients are derived as follows:

$$a = \frac{s^+_{xy} - s^-_{xy}}{2T_{\rm oss}} \tag{16}$$

$$b = s^-_{xy} \tag{17}$$

$$c = \begin{cases} -I_{xy}, & \text{for the primary side} \\ I_{xy}, & \text{for the secondary side.} \end{cases} \tag{18}$$

Meanwhile, during diode current commutation, the slope of the current remains consistent as $s^+_{xy}$. Therefore, the current is

calculated as a linear function of time as follows:

$$i_L(t) = a'(t - T_{\text{oss}}) + b' \quad (T_{\text{oss}} \le t < T_{\text{dt}}) \tag{19}$$

where the coefficients are derived from the continuity of the current as follows:

$$a' = s_{xy}^{+} \tag{20}$$

$$b' = \begin{cases} \frac{(s_{xy}^{-}+s_{xy}^{+})T_{\text{oss}}}{2} - I_{xy}, & \text{for the primary side} \\ \frac{(s_{xy}^{-}+s_{xy}^{+})T_{\text{oss}}}{2} + I_{xy}, & \text{for the secondary side.} \end{cases} \tag{21}$$

### D. Accurate Solutions for Minimum ZVS-Current

To accurately determine the ZVS-current, the proposed inductor current approximation is applied, incorporating the ZVS requirements outlined in Section III-B and illustrated in Fig. 8. First, the condition for initiating the ZVS process, where $I_{xy}$ satisfies (11), is given by

$$I_{xy} \ge 0. \tag{22}$$

Next, to achieve complete resonance between $L$ and $C_{\text{oss}}$ within the dead time, the ZVS-current is derived using the proposed inductor current approximation from (15). For the primary-side switches, $T_{\text{oss}}$ can be calculated from

$$\begin{aligned} \int_0^{T_{\text{oss}}} i_L(t)dt &= \frac{1}{3}aT_{\text{oss}}^3 + \frac{1}{2}bT_{\text{oss}}^2 + cT_{\text{oss}} \\ &= \frac{2s_{xy}^{-} + s_{xy}^{+}}{6}T_{\text{oss}}^2 - I_{xy}T_{\text{oss}} \\ &= -2Q_{\text{oss}}(V_p). \end{aligned} \tag{23}$$

Substituting (23) into (12), the condition for $I_{xy}$ to satisfy (12) for the primary side is obtained as follows:

$$I_{xy} \ge I_{xy,\text{zvs}}^{\text{ch}} \triangleq \frac{2Q_{\text{oss}}(V_p)}{T_{\text{dt}}} + \frac{2s_{xy}^{-} + s_{xy}^{+}}{6}T_{\text{dt}} \tag{24}$$

where $I_{xy,\text{zvs}}^{\text{ch}}$ refers to the ZVS-current based on charge exchange, considering the dynamic circuit behavior during the dead time.

Since the direction of the current is inverted and its magnitude is $n$ times larger for the secondary side, the ZVS condition for the secondary-side switch is obtained as follows:

$$I_{xy} \ge I_{xy,\text{zvs}}^{\text{ch}} \triangleq \frac{2Q_{\text{oss}}(V_s)}{nT_{\text{dt}}} - \frac{2s_{xy}^{-} + s_{xy}^{+}}{6}T_{\text{dt}}. \tag{25}$$

To maintain a consistent current direction during the dead time, the ZVS-current is further refined using the proposed current approximation. (13) can be rewritten as

$$i_L(T_{\text{dt}}) = -I_{xy} + \frac{s_{xy}^{-} + s_{xy}^{+}}{2}T_{\text{dt}} \le 0 \text{ for both sides.} \tag{26}$$

This formulation ensures $T_{\text{oss}} = T_{\text{dt}}$, minimizing the body diode commutation period during the dead time. By reducing the turn-OFF current of switch $S_{p2}$, ZVS operation is enhanced across a broader range of operating conditions while limiting body diode conduction losses. Consequently, the ZVS-current considering the dead time and the prevention of re-resonance during body diode commutation, $I_{xy,\text{zvs}}^{\text{dt}}$, is derived as

$$I_{xy,\text{zvs}}^{\text{dt}} \triangleq \frac{s_{xy}^{-} + s_{xy}^{+}}{2}T_{\text{dt}} \text{ for both sides.} \tag{27}$$

Thus, the required ZVS-current for each switch to achieve complete ZVS, $I_{xy,\text{zvs}}$, is determined as

$$I_{xy,\text{zvs}} = \max\left\{0, I_{xy,\text{zvs}}^{\text{ch}}, I_{xy,\text{zvs}}^{\text{dt}}\right\}. \tag{28}$$

Based on the specifications of the DAB converter summarized in Table III, the ZVS-current of each switch under different operating conditions is calculated, as illustrated in Fig. 9. Considering the switching device characteristics, the dead time is set to $T_{\text{dt}} = 300$ ns, with the diode commutation period minimized by reducing the required ZVS-current. By dynamically adjusting the ZVS-current according to the operating conditions, as depicted in Fig. 9, precise ZVS criteria are established. This

TABLE III
SPECIFICATIONS OF THE DAB CONVERTER HARDWARE

| Parameter | Value |
|---|---|
| Input voltage $V_p$ | 600 V–800 V |
| Output voltage $V_s$ | 300 V–500 V |
| Rated power $P_{\text{rated}}$ | 20 kW |
| Transformer specifications | Leakage inductance $L$ 28 µH |
| | Turns ratio $n$ 1.875 |
| | Pri. 15 turns (7.3 mΩ) |
| | Sec. 8 turns (4.0 mΩ) |
| | Litz wire 0.12 mm*1000 strands |
| | Core 0R49928EC*6EA |
| | Magnetizing inductance $L_m$ 3.74 mH |
| Switches $S_{xy}$ | SiC MOSFET IMZA120R007M1H |
| Buffer capacitor | 8*20 µF |
| Controller | TMS320F28377D |
| Switching frequency $f_{sw}$ | 50 kHz |
| Dead time $T_{\text{dt}}$ | 300 ns |

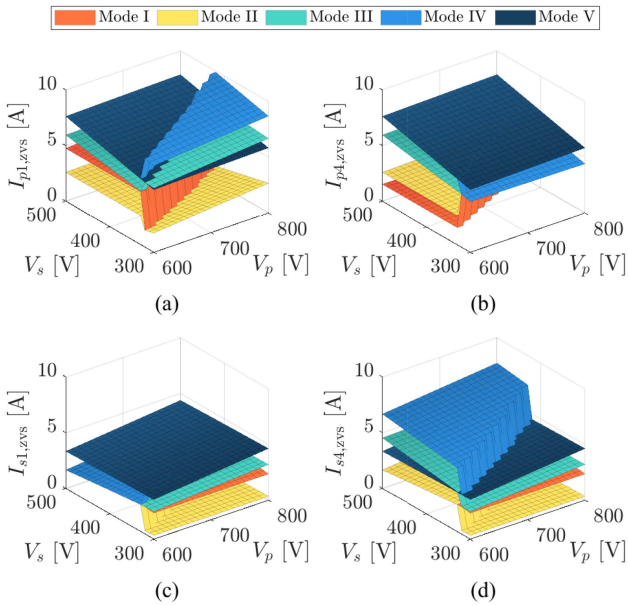


Fig. 9. ZVS-current $I_{xy,\text{zvs}}$ for switch $S_{xy}$ under each operating mode for wide operating voltages when $T_{\text{oss}} = T_{\text{dt}}$. (a) $S_{p1}$. (b) $S_{p4}$. (c) $S_{s1}$. (d) $S_{s4}$.

approach effectively expands the ZVS range while minimizing the associated increase in rms current.

## IV. Proposed ZVS-Enhanced and RMS-Current-Minimized Optimal TPS Modulation

Building on the accurate ZVS-current calculations that account for dynamic circuit behavior during the dead time, the proposed TPS modulation enhances the efficiency of the DAB converter by maximizing ZVS capability with minimal increase in circulating power.

### A. ZVS Capability in the Operating Regions

This article presents an accurate calculation of ZVS-currents to maximize ZVS capability. ZVS region is analyzed through nonlinear optimization, identifying the operating boundaries for the three distinct regions. These boundaries are determined by finding the supremum and infimum operating powers where all switches achieve ZVS, considering the number of ZVS-enabled switches and operating modes I-V. The optimization problem is formulated as follows:

$$\min_{\mathbf{x}} f_o(\mathbf{x}) \,\text{s.t.}\, \begin{cases} \mathbf{A}\mathbf{x} \le \mathbf{b}, & \mathbf{A}_{\text{eq}}\mathbf{x} = \mathbf{b}_{\text{eq}} \\ \mathbf{c}(\mathbf{x}) \le \mathbf{0}, & \mathbf{c}_{\text{eq}}(\mathbf{x}) = \mathbf{0} \\ \mathbf{lb} \le \mathbf{x} \le \mathbf{ub} \end{cases} \tag{29}$$

where $\mathbf{x} \triangleq [D_p\ D_s\ D_\phi]^\top$ represents the control variables, $c(\mathbf{x})$ and $c_{\text{eq}}(\mathbf{x})$ denote nonlinear constraints, and $(\mathbf{A}, \mathbf{b})$ and $(\mathbf{A}_{\text{eq}}, \mathbf{b}_{\text{eq}})$ define linear constraints. The linear constraints are specified from the mode constraints and the ZVS constraints as detailed in Table I. The boundary conditions for $\mathbf{x}$ consist of the lower boundary $\mathbf{lb} = [0\,0\,0]^\top$, and the upper boundary $\mathbf{ub} = [0.5\ 0.5\ 0.25]^\top$.

To determine the supremum power for achieving all-ZVS operation in the light-load region, denoted as $P^{\text{zvs}}_{\text{sup},ll}$, the objective function $f_o$ is set as the output power $P_o(\mathbf{x})$ using (7). The constraints for achieving all-ZVS in mode II are defined by the mode constraints in Table I and the ZVS condition $I_{xy} \ge I^{\text{II}}_{xy,\text{zvs}}$, to ensure complete ZVS. Similarly, to find the infimum operating power of all-ZVS achievable in the heavy-load region, denoted as $P^{\text{zvs}}_{\text{inf},hl}$, $f_o$ is set as $-P_o(\mathbf{x})$, with the mode and ZVS constraints for mode IV operation, as specified in Table I.

Fig. 10 illustrates the ZVS region with maximized ZVS capability for $V_p = 600$ V and 800 V, while other parameters given in Table III. The results indicate that all-ZVS operation is only achievable either below $P^{\text{zvs}}_{\text{sup},ll}$ (light load) or above $P^{\text{zvs}}_{\text{inf},hl}$ (heavy load). In the light-load all-ZVS region, the operating mode transitions from mode I to mode II as load increases. Likewise, in the heavy-load all-ZVS region, the operating mode shifts from mode IV to mode V. In the medium-load range, where achieving all-ZVS is infeasible, a six-ZVS strategy is employed to maximize the number of ZVS-enabled switches and minimize switching losses. Here, the operating mode transitions from mode II to mode III.

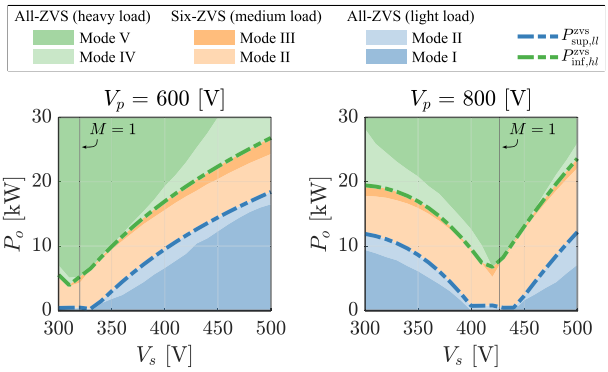


Fig. 10. ZVS region of the proposed modulation scheme with enhanced ZVS capability, illustrated for $V_p = 600$ V and 800 V. The boundary between buck- and boost-type operations is marked at $M = 1$.

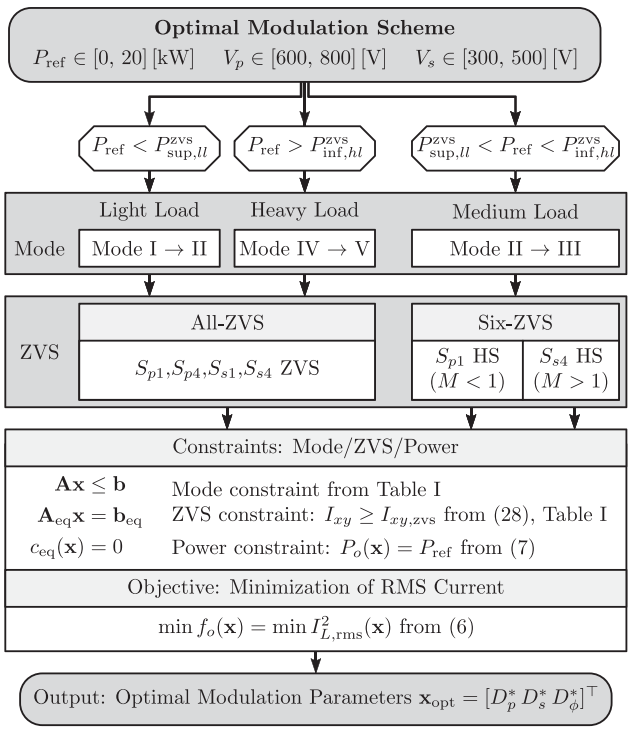


Fig. 11. Summary of the proposed TPS modulation to derive optimal modulation parameters for maximum number of ZVS-achieved switches and minimization of rms currents.

### B. Proposed Optimal Modulation Scheme

Based on the derivation of the ZVS region, the optimal modulation parameters for the proposed rms-current-minimized and ZVS-enhanced TPS modulation are determined, as outlined in Fig. 11. The optimization process is conducted using "`fmincon`" nonlinear optimization solver in MATLAB to obtain the optimal solution for specified operating voltage ranges and power ratings. The procedure is as follows.

1) *The ZVS type (all-ZVS or six-ZVS) and the operating mode* are identified based on the maximized ZVS region.
2) *Linear constraints*, $(\mathbf{A}, \mathbf{b})$ and $(\mathbf{A}_{\text{eq}}, \mathbf{b}_{\text{eq}})$, are set as mode and ZVS constraints based on the categorization
   a) *All-ZVS:* Include ZVS constraints for all switches.

TABLE IV
OPTIMIZATION FOR ALL-ZVS OPERATION UNDER BUCK-TYPE MODE I

| | |
|---|---|
| Mode constraint | $D_s - D_p < 2D_\phi \wedge D_p < D_s < 0.5$ |
| ZVS constraint | $I_{p1} = \frac{V_p}{2f_sL}[(1-M)D_p - 2MD_\phi] > I_{p1,\text{zvs}}^{\text{I-buck}}$<br>$I_{p4} = \frac{V_p}{2f_sL}[(1-M)D_p + 2MD_\phi] > I_{p4,\text{zvs}}^{\text{I-buck}}$<br>$I_{s1} = \frac{V_p}{2f_sL}[-D_p + MD_s] > I_{s1,\text{zvs}}^{\text{I-buck}}$<br>$I_{s4} = \frac{V_p}{2f_sL}[-D_p + MD_s] > I_{s4,\text{zvs}}^{\text{I-buck}}$ |
| Power constraint | $P_o(\mathbf{x}) = \sum_{h=1,3,5} P_h = P_{\text{ref}}$ |
| Objective function | $I_{L,\text{rms}}^2(\mathbf{x}) = \frac{1}{2}\sum_{h=1,3} \lvert\vec{I}_{L,h}\rvert^2$ |

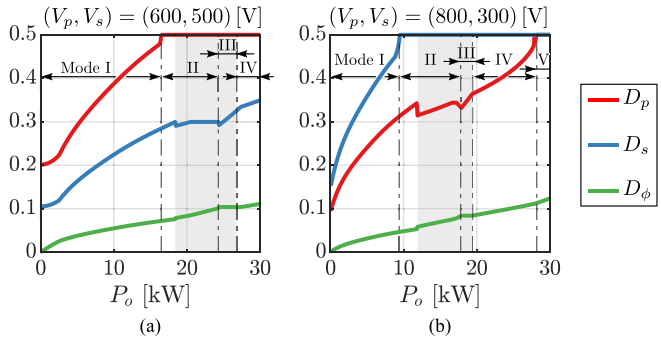


Fig. 12. Optimal modulation parameters obtained for the edge operating points. (a) Boost-type operation $(V_p, V_s) = (600, 500)$ V, where $M = 1.56$. (b) Buck-type operation $(V_p, V_s) = (800, 300)$ V, where $M = 0.7$.

b) *Six-ZVS:* Exclude the ZVS constraint for the switch that cannot achieve ZVS, where hard-switching is applied instead. Depending on the voltage ratio $M$, either $S_{p1}$ or $S_{s4}$ loses ZVS capability for buck- or boost-type operation, respectively.

3) *Nonlinear constraint*, $c_{\text{eq}}(\mathbf{x}) = 0$, is specified as a power constraint to ensure the desired power output, i.e., $P_o(\mathbf{x}) = P_{\text{ref}}$, where $P_{\text{ref}}$ is the reference power.
4) *Objective function*, $f_o(\mathbf{x})$, is defined as the rms current, considering both the 1st and 3rd harmonic components, as defined in (6).
5) *Optimal modulation parameters* $\mathbf{x}_{\text{opt}}$ are obtained by minimizing the rms current (step 4) while satisfying the constraints in steps 2 and 3.

As an example, Table IV summarizes the constraints and objective function for all-ZVS operation under buck-type mode I, where $I_{xy,\text{zvs}}^{\text{I-buck}}$ represents the ZVS-current of switch $S_{xy}$ in this mode.

For practical implementation, the optimization is performed using ZVS-currents $I_{xy,\text{zvs}}$ calculated for $T_{\text{oss}} = 0.5T_{\text{dt}}$. This approach ensures sufficient energy for ZVS accounting for uncertainties in parasitic components and actual dead time in switching legs, while minimizing excessive circulating currents.

Figs. 12 and 13 illustrate the optimal modulation parameters and the corresponding inductor currents for both buck- and boost-type operations. As output power increases, the operation transitions from light-load all-ZVS (modes I to II) to six-ZVS

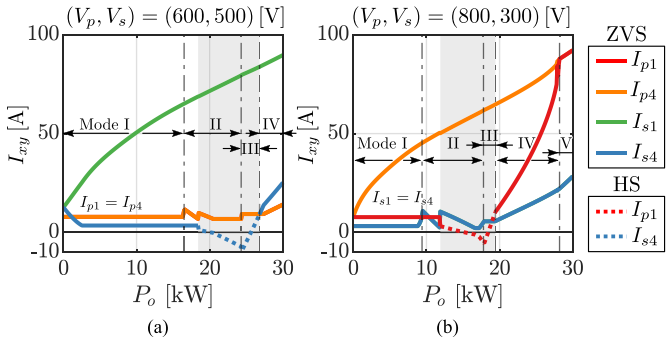


Fig. 13. Optimized inductor currents obtained for the edge operating points. (a) Boost-type operation $(V_p, V_s) = (600, 500)$ V, where $M = 1.56$. (b) Buck-type operation $(V_p, V_s) = (800, 300)$ V, where $M = 0.7$.

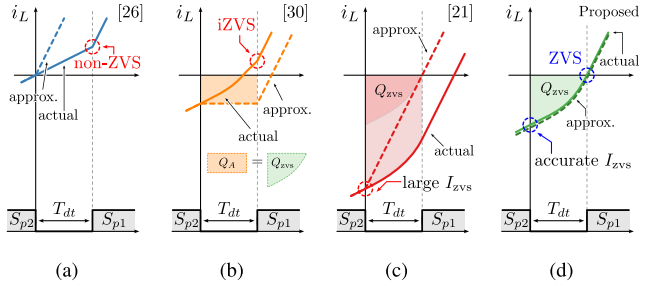


Fig. 14. Comparison on different approximation methods to derive ZVS-current for ZVS operation based on different considerations. (a) Direction of current [26]. (b) Charge in equivalent capacitors [30]. (c) Effect of dead time [21]. (d) Proposed method, considering dynamic behavior of current during the dead time.

(mode II to mode III) in shaded area, and finally to heavy-load all-ZVS (mode IV → V). In the six-ZVS region, as shown in Fig. 13(a), $S_{s4}$ fails to achieve ZVS in boost-type operation due to insufficient inductor current, where $I_{s4}$ smaller than the required ZVS-current. Similarly, $S_{p1}$ loses ZVS capability for buck-type operation, as illustrated in Fig. 13(b). However, all other switches successfully achieve ZVS, as their currents exceed the required ZVS thresholds.

### C. Comparison With Other TPS Modulations

To validate the effectiveness of the proposed method, a comprehensive comparison with existing TPS modulation schemes from the literature is presented in Table V. Among them, the modulation scheme in [22] does not impose ZVS constraints, while other approaches differ in their methods of enhancing ZVS. The simplest approach determines ZVS operation based on current direction [26], as illustrated in Fig. 14(a). However, since it does not account for charge exchange and dead time, ZVS may not always be achieved, resulting in non-ZVS (i.e., hard switching), as described in Fig. 14(a). Charge-exchange-based methods assume a constant inductor current during the dead time [30], equating the charge transfer to the required ZVS charge, as depicted in Fig. 14(b). However, because inductor current varies dynamically during dead time, this assumption can lead to unintentional incomplete ZVS (iZVS). To address this,

TABLE V
PROPOSED OPTIMAL MODULATION SCHEME WITH OTHER EXISTING APPROACHES

| Modulation | Hardware Specification | Peak Efficiency | Optimization Target | Considerations for ZVS | | | | | ZVS Capability |
|---|---|---|---|---|---|---|---|---|---|
| | | | | Direction of current | Energy-charge | Inductor voltage | Dead time | Dynamic circuit behavior | |
| TPS [22] | 600–800 V to 200–450 V 5 kW/80 kHz | 95.9% | RMS current | No | No | No | No | No | Two-ZVS (light) All-ZVS (heavy) NA (medium) |
| OCS-TPS [26] | 100 V to 50–200 V 960 W/100 kHz | 96.4% | Current stress | Yes | No | No | No | No | All-ZVS (light/heavy) NA (medium) |
| FDM [19] | 200 V to 100–200 V 1 kW/50 kHz | $<96\%$ | RMS current | Yes | Yes | No | No | No | All-ZVS (light/heavy) NA (medium) |
| NSGA-II TPS [30] | 400 V to 300 V 3.3 kW/150 kHz | 97% | RMS current, current stress | Yes | Yes | No | No | No | All-ZVS (light/heavy) NA (medium) |
| SPS/DPS [28] | 120 V to 80 V 600 W/100 kHz | 96% | Current stress | Yes | No | No | Yes | No | Four-ZVS (light) All-ZVS (medium/heavy) |
| OTPS [23] | 60–200 V to 110 V 400 W/10 kHz | 95.7% | RMS current | Yes | Yes | Yes | No | No | All-ZVS (light/heavy) Four-ZVS (medium) |
| TPS [21] | 160–320 V to 160-390 V 4.5 kW/100 kHz | 96.3% | RMS current | Yes | Yes | Yes | Yes | No | All-ZVS (light/heavy) Six-ZVS (medium) |
| TPS [25] | 380 V to 0–380 V 1.5 kW/50 kHz | 97.6% | Current stress | Yes | Yes | Yes | Yes | No | All-ZVS (light/heavy) Six-ZVS (medium) |
| **Proposed** | **600–800 V to 300–500 V 20 kW/50 kHz** | **98.8%** | **RMS current** | **Yes** | **Yes** | **Yes** | **Yes** | **Yes** | **All-ZVS (light/heavy) Six-ZVS (medium)** |

the method in [21] accounts for both dead-time effects and inductor voltage (i.e. the slope of current) to prevent re-resonance and iZVS, achieving complete ZVS as illustrated in Fig. 14(c). However, this approach overestimates the required ZVS-current, resulting in excessive circulating power that degrades efficiency, particularly under light-load conditions. In contrast to the aforementioned approaches, the proposed method precisely calculates the ZVS-current, as shown in Fig. 14(d), ensuring complete ZVS while minimizing unnecessary circulating current.

The effectiveness of this accurate ZVS-current calculation is demonstrated by comparing the rms current of the proposed method with state-of-the-art rms-minimized TPS modulation schemes from [21] and [22]. Fig. 15(a) and (b) illustrates the rms currents under boost- and buck-type operations, respectively, where $P^* := P_o/P_{\text{rated}}$ represents the per-unit power with a base transmission power of $P_{\text{rated}} = 20$ kW. The modulation scheme in [21] employs excessively large ZVS-currents, leading to higher rms currents due to increased circulating current. Conversely, the scheme in [22] achieves the lowest rms currents among the compared methods but does not guarantee maximum efficiency. The absence of a nonzero ZVS-current results in hard switching, degrading overall performance. The proposed method strikes an optimal balance by significantly reducing rms current compared to [21] through precise ZVS-current calculation, while preserving ZVS capability. This minimizes excessive circulating current, reducing conduction losses associated with ZVS enhancement.

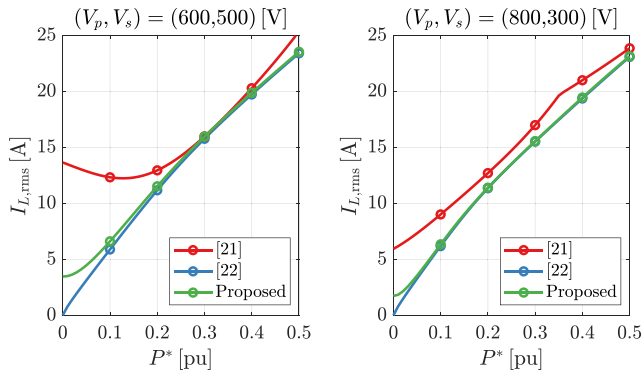


Fig. 15. Comparison on the rms current of different modulation schemes. (a) Boost-type operation $(V_p, V_s) = (600, 500)$ V, where $M = 1.56$. (b) Buck-type operation $(V_p, V_s) = (800, 300)$ V, where $M = 0.7$.

Beyond minimizing conduction loss, accurate ZVS-current calculation also reduces switching loss by expanding the all-ZVS region, as shown in Fig. 16. As highlighted in Table V, while most TPS modulation schemes in prior studies achieve all-ZVS under light- and heavy-load conditions, many do not account for ZVS operation under medium-load conditions, where all-ZVS operation is infeasible. In these cases, six-ZVS is adopted in [21] and [25] to maximize the number of switches achieving ZVS. However, in [21], excessive margin applied to ZVS-current constraints underestimates the all-ZVS region,

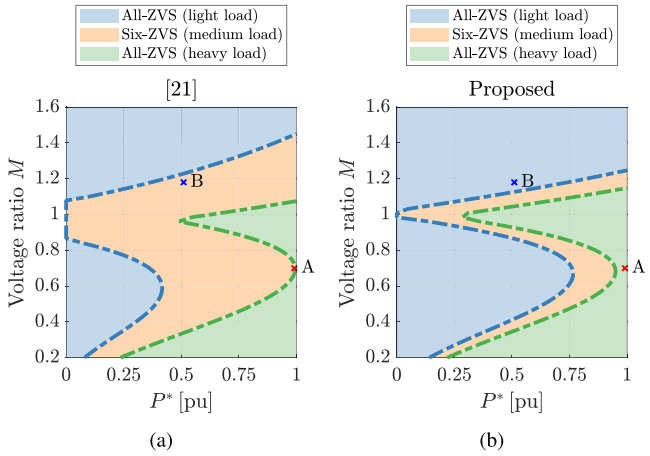


Fig. 16. Comparison on ZVS capability of different modulation schemes when $V_p = 800$ V, where A denotes the operating point (1 pu, 0.7) and B denotes (0.5 p.u., 1.18). (a) For the operating points A and B, six-ZVS is achieved with modulation scheme in [21]. (b) For the points A and B, all-ZVS is achieved with the proposed modulation scheme.

as depicted in Fig. 16(a). In contrast, the proposed method, leveraging accurate ZVS-current calculations, expands the all-ZVS region, as shown in Fig. 16(b). At operating points A $(P^* = 1\,\text{pu}, M = 0.7)$ and B $(P^* = 0.5\,\text{pu}, M = 1.18)$, all-ZVS is achieved with the proposed method, whereas six-ZVS is observed for the scheme in [21].

The efficiency of each method summarized in Table V is heavily influenced by hardware specifications such as power ratings, switching frequencies, and power devices. In some cases, efficiency is constrained by hardware limitations rather than modulation schemes. For instance, the method in [21] employs 1200-V SiC MOSFETs (IMZ120R030M1H) for both the primary- and secondary-side switches. This leads to suboptimal efficiency, as the device voltage rating (1200 V) far exceeds the actual operating voltage (below 400 V). In contrast, [25] utilizes 650-V SiC MOSFETs (SCT3060AR), which better match the operating conditions and thus achieve higher efficiency.

To ensure a fair comparison, the state-of-the-art modulation schemes from [21] and [22] are implemented using the same power hardware as the proposed method. Their efficiencies are experimentally measured under identical conditions. The precise ZVS-current calculation of the proposed method improves its feasibility for practical implementation by balancing rms current minimization and ZVS performance. This balance leads to enhanced overall efficiency, as further discussed in Section V.

## V. Experimental Results

For the experimental verification of the proposed modulation scheme, a 20 kW/50 kHz SiC-based DAB converter hardware was built, as shown in Fig. 17. The DAB converter was controlled using a TMS320F28377 DSP, while a LeCroy HDO8108 oscilloscope and a Yokogawa WT-5000E power analyzer were used to measure operating waveforms and efficiency, respectively. The detailed specifications of the DAB converter are summarized in Table III.

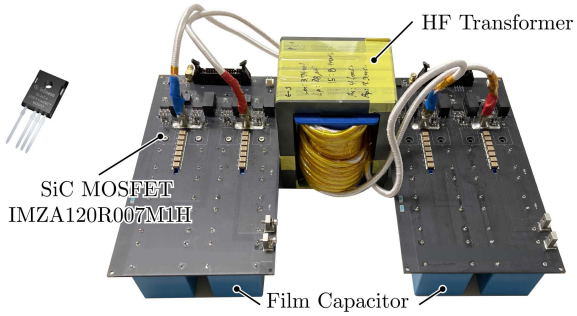


Fig. 17. 20 kW/50 kHz SiC-based DAB converter hardware.

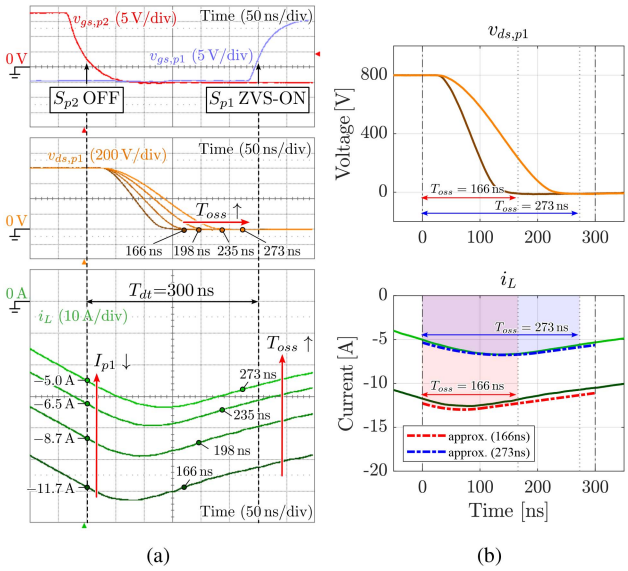


Fig. 18. Dynamic behavior of current during the dead time when $T_{\text{oss}}$ varies as 166 ns, 198 ns, 235 ns, and 273 ns, with decreasing $I_{p1}$, where $V_p = 800$ V and $V_s = 300$ V. (a) Experimental waveforms of $v_{\text{ds},p1}$ and inductor current during the dead time. (b) Comparison of the experimental results (solid lines) with the proposed approximation (dashed lines).

This section first validates the accuracy of the proposed inductor current approximation during the dead time by comparing experimental current waveforms with the predicted values. Next, a comparative analysis of steady-state operating waveforms is conducted to assess rms current and ZVS capability, demonstrating the effectiveness of the proposed TPS modulation scheme. Finally, measured efficiency results highlight the efficiency improvements achieved with the proposed method.

### A. Verification of Accurate ZVS-Current Calculation

Fig. 18(a) presents an experimental waveform illustrating the inductor current dynamics during the dead time when $S_{p2}$ turns OFF and $S_{p1}$ subsequently turns ON in buck-type mode I operation. The waveforms are obtained employing the proposed modulation scheme with varying $T_{\text{oss}}$ values in the ZVS-current calculation. When a longer $T_{\text{oss}}$ is used, the turn-OFF current of $S_{p2}$ is smaller, requiring more time for the resonant transition to fully charge and discharge the parasitic capacitors. As the absolute value of the turn-OFF current $I_{p1}$ decreases from 11.7 to

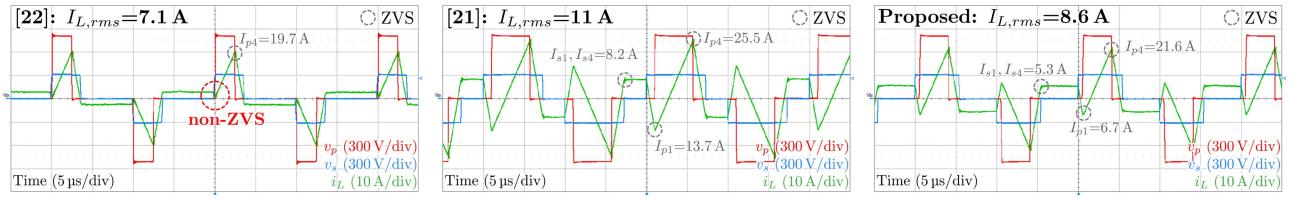


(a) (b) (c)

Fig. 19. Waveforms of buck-type mode I operation for $V_p = 800$ V and $V_s = 300$ V ($M = 0.7$), where $P^* = 0.1$ pu ($P_o = 2$ kW). (a) TPS modulation in [22]. (b) TPS modulation in [21]. (c) Proposed modulation scheme.

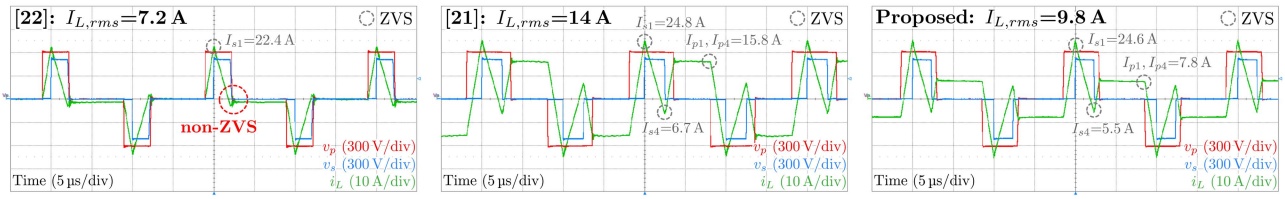


(a) (b) (c)

Fig. 20. Waveforms of boost-type mode I operation for $V_p = 600$ V and $V_s = 500$ V ($M = 1.56$), where $P^* = 0.1$ pu ($P_o = 2$ kW). (a) TPS modulation in [22]. (b) TPS modulation in [21]. (c) Proposed modulation scheme.

5.0 A, the resonance time $T_{\rm oss}$ increases from 166 to 273 ns, as shown in Fig. 18(a). This experimentally observed behavior confirms the close relationship between ZVS-current and the achievement of complete ZVS, highlighting the importance of accurate ZVS-current calculation.

In Fig. 18(b), the drain-source voltage $v_{{\rm ds},p1}$ and the inductor current $i_L$ from Fig. 18(a) are plotted alongside the proposed approximation of the dynamic current. The approximated waveforms of $i_L$ are represented by red and blue dashed lines for $T_{\rm oss} = 166$ ns and 273 ns, respectively. Here, $i_L$ is modeled as a piecewise combination of quadratic and linear functions, as proposed in Section III. The red and blue shaded areas in the bottom inset of Fig. 18(b) correspond to the charge required for complete $C_{\rm oss}$ discharge to achieve complete ZVS. The close agreement between the experimental and approximated waveforms validates the accuracy of the proposed ZVS-current calculation, which effectively accounts for dynamic current behavior during the dead time.

### B. Steady-State Operating Waveforms

This section highlights the minimal circulating current required for all-ZVS operation using the proposed method by comparing steady-state waveforms under both buck- and boost-type operations with those from state-of-the-art modulation schemes. By leveraging precise ZVS-current calculation, the proposed method ensures complete ZVS with minimal increase in circulating current.

Fig. 19 illustrates the operating waveforms of each modulation scheme at $(V_p, V_s) = (800, 300)$ V ($M = 0.7$), and $P^* = 0.1$ pu ($P_o = 2$ kW). When only rms current is minimized without considering ZVS [22], as shown in Fig. 19(a), the lowest rms current of 7.1 A, is achieved. However, only two switches $S_{p3}$ and $S_{p4}$ achieve ZVS, leading to increased switching losses. Conversely, in Fig. 19(b), when the ZVS-current is overestimated with excessive margin [21], the rms current rises to 11 A, enabling all-ZVS operation but at the cost of higher conduction losses. In contrast, the proposed method achieves all-ZVS with minimal circulating current, resulting an rms current of 8.6 A, as depicted in Fig. 19(c), which is 22% lower than the all-ZVS scenario in 19(b).

Similarly, Fig. 20 presents the operating waveforms at $(V_p, V_s) = (600, 500)$ V ($M = 1.56$), and $P^* = 0.1$ pu ($P_o = 2$ kW). In Fig. 20(a), the lowest rms current of 7.2 A is achieved, but only two switches achieve ZVS, resulting in higher switching losses. In Fig. 20(b), excessive ZVS-current calculation leads to all-ZVS operation, but with a significantly increased rms current of 14 A. The proposed method, as shown in Fig. 20(c), achieves all-ZVS with an rms current of 9.8 A, which is 30% lower than the rms current in Fig. 20(b).

### C. Characteristic Waveforms of ZVS Operation

Accurate ZVS-current constraints not only reduce rms current for ZVS operation, but also expand the ZVS region, as discussed in Section IV-C. To verify the enhanced ZVS capability of the proposed method, the inductor current ($i_L$), gate-source voltage ($v_{\rm gs}$), and drain-source voltage ($v_{\rm ds}$) were measured for each switch. The operating points A and B are marked in Fig. 16, where point A refers to the buck-type operation with $(V_p, V_s) = (800, 300)$ V ($M = 0.7$) and $P^* = 1$ pu ($P_o = 20$ kW); and point B refers to the boost-type operation with $(V_p, V_s) = (800, 500)$ V ($M = 1.18$) and $P^* = 0.5$ pu ($P_o = 10$ kW).

Fig. 21 illustrates the ZVS waveforms at the buck-type operating point A. This point lies within the six-ZVS region near the ZVS boundary in Fig. 16(a) due to excessive margin in

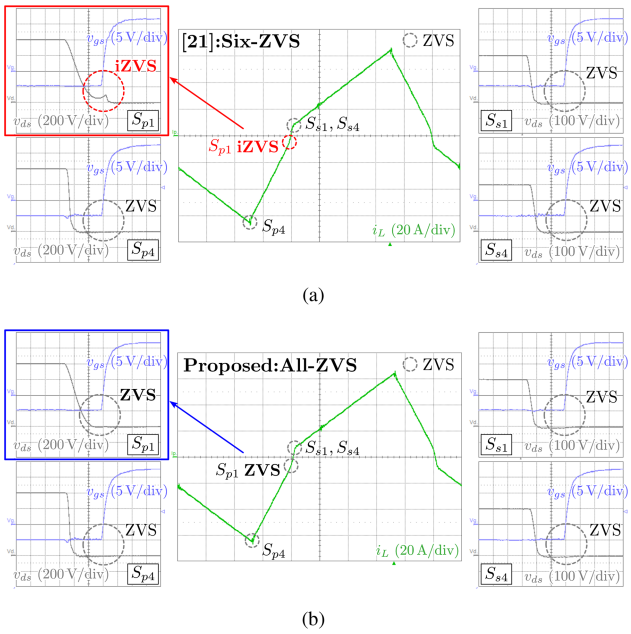


Fig. 21. ZVS waveforms compared at operating point **A** in Fig. 16: $(V_p, V_s) = (800, 300)$ V ($M = 0.7$) and $P^* = 1$ pu ($P_o = 20$ kW). (a) Six-ZVS achieved using modulation in [21]. (b) All-ZVS achieved with the proposed method.

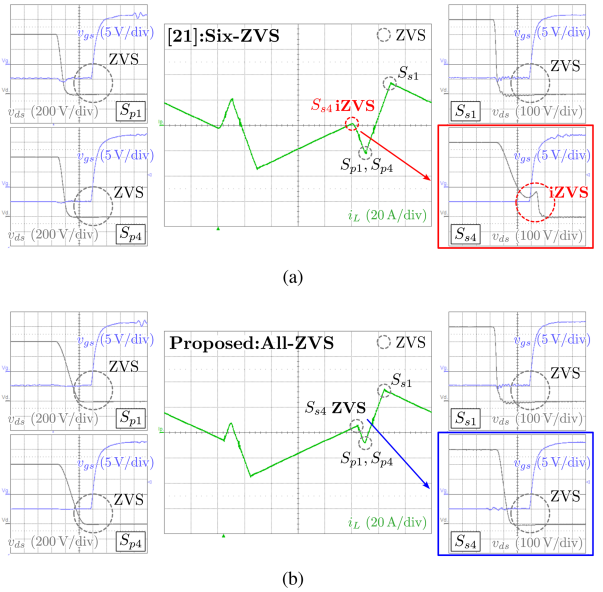


Fig. 22. ZVS waveforms compared at operating point **B** in Fig. 16: $(V_p, V_s) = (800, 500)$ V ($M = 1.18$) and $P^* = 0.5$ pu ($P_o = 10$ kW). (a) Six-ZVS achieved using modulation in [21]. (b) All-ZVS achieved with the proposed method.

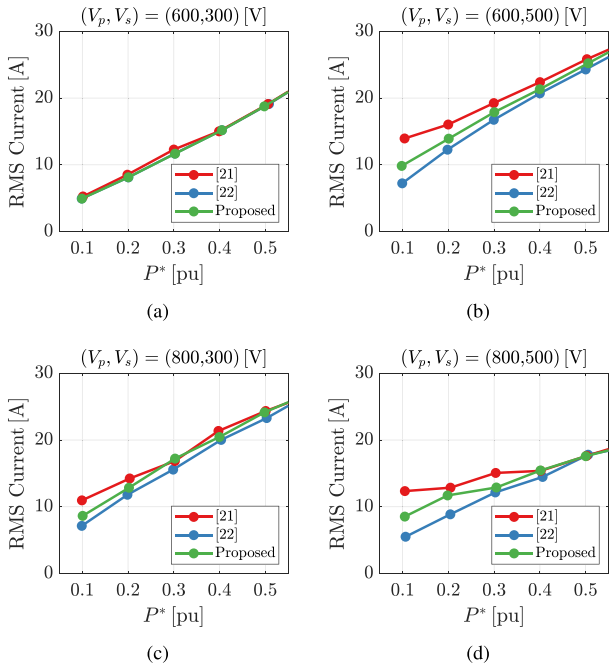


Fig. 23. Experimentally measured rms inductor current curves of the proposed methods and the TPS modulation schemes in [21] and [22], at the edge operating voltages. (a) $(V_p, V_s) = (600, 300)$ V, where $M = 0.94$. (b) $(V_p, V_s) = (600, 500)$ V, where $M = 1.56$. (c) $(V_p, V_s) = (800, 300)$ V, where $M = 0.7$. (d) $(V_p, V_s) = (800, 500)$ V, where $M = 1.18$.

the ZVS-current calculation. Therefore, achieving all-ZVS is deemed infeasible with the modulation method in [21], and the optimal modulation parameters are derived under this assumption to minimize inductor current. As shown in Fig. 21(a), the primary-side switch $S_{p1}$ fails to achieve complete ZVS, reaching iZVS, where $v_{\rm gs}$ begins rising before $v_{\rm ds}$ has fully dropped to zero. This incomplete ZVS is due to an insufficient current caused by inaccurate ZVS-current calculations. However, with the accurate ZVS criteria and maximized ZVS capability of the proposed method, the same point shifts to heavy-load all-ZVS region in Fig. 16(b). As a result, Fig. 21(b) shows that the proposed method achieves complete ZVS for all switches under buck-type mode IV operation.

Fig. 22 presents the ZVS waveforms at the boost-type operating point B. Similar to point A, point B lies within the six-ZVS region near the ZVS boundary in Fig. 16(a) due to inaccurate ZVS-current calculation. As depicted in Fig. 22(a), the secondary-side switch $S_{s4}$ fails to achieve ZVS, instead reaching iZVS. However, with the accurate ZVS criteria of the proposed method, this point moves into the light-load all-ZVS region in Fig. 16(b). Consequently, Fig. 22(b) confirms that the proposed method enables complete ZVS for all switches under boost-type mode II operation.

In summary, the proposed method maximizes ZVS capability in practice, ensuring complete ZVS across all switches and thereby reducing switching losses.

### *D. RMS Currents and Efficiencies*

Fig. 23 compares the experimentally measured rms currents of the proposed method with those of the TPS modulation schemes in [21] and [22], evaluated under edge operating voltages. The scheme in [21] exhibits the highest rms currents, primarily due to excessive margin in ZVS-current calculations, which significantly increases rms current. In contrast, the method in [22] achieves the lowest rms current by eliminating circulating power. However, it neglects ZVS in the optimization process, leading to increased switching losses from hard switching. Unlike these approaches, the proposed method accurately determines the

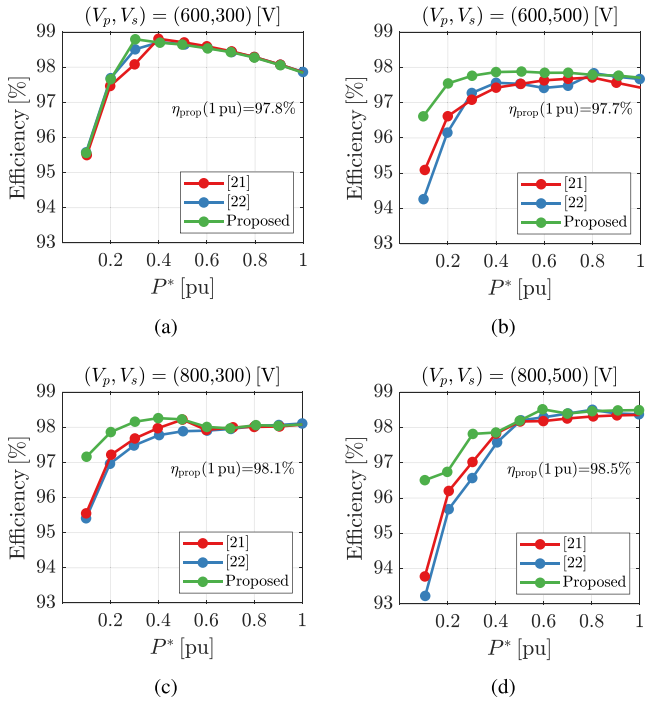


Fig. 24. Experimentally measured efficiency curves of the proposed methods and the TPS modulation schemes in [21] and [22], at the edge operating voltages. (a) $(V_p, V_s) = (600, 300)$ V, where $M = 0.94$. (b) $(V_p, V_s) = (600, 500)$ V, where $M = 1.56$. (c) $(V_p, V_s) = (800, 300)$ V, where $M = 0.7$. (d) $(V_p, V_s) = (800, 500)$ V, where $M = 1.18$.

minimal required ZVS-current and circulating power to achieve ZVS, effectively reducing both conduction and switching losses. As a result, the rms current of the proposed method falls between those of the other two schemes, aligning with the analysis in Section IV-C. For buck-type mode I operation at $(V_p, V_s) = (800, 300)$ V, the proposed method calculates ZVS-currents of $I_{p1} = 6.7$ A and $I_{s1} = 5.3$ A for the primary and secondary sides, respectively. These values reduce unnecessary circulating power compared to the ZVS-currents computed in [21], where $I_{p1} = 13.7$ A and $I_{s1} = 8.2$ A are used. Consequently, both rms and switching currents in the proposed method are significantly lower than in [21], leading to reduced conduction and switching losses.

Fig. 24 shows the experimentally measured efficiency curves for the proposed method and the compared TPS modulation schemes. In most operating conditions, the proposed method achieves the highest efficiency, except at $(V_p, V_s) = (600, 300)$ V where the voltage conversion ratio approaches unity ($M = 0.95$), as depicted in Fig. 24(a). Compared to [22], the proposed method significantly enhances efficiency by minimizing switching losses through complete ZVS operation without a notable increase in rms current. Furthermore, the proposed method outperforms the scheme in [21], especially under light-load conditions. In these conditions, the impact of conduction losses from circulating current during ZVS operation have a large impact on efficiency. For instance, at $P^* = 0.1$ pu, the proposed method achieves an efficiency of 97.16% for buck-type operation at $(V_p, V_s) = (800, 300)$ V, which is 1.61%p and 1.75%p higher than the compared TPS modulation schemes [21] and [22] respectivly, as depicted in Fig. 24(c). As a result, due to significant enhancement in light-load efficiency, the proposed method attained the average measured efficiency of 97.9% for the entire load range at the edge operating voltages, which is 0.3%p and 0.4%p higher than those of the compared schemes.

In summary, the experimental results validate the superior performance of the proposed method, demonstrating its ability to achieve high efficiency through optimized ZVS operation with minimal circulating power.

## VI. Conclusion

This article presents a TPS modulation scheme designed to enhance the efficiency of a DAB converter by incorporating precise ZVS criteria. The operating modes and load regions are systematically categorized based on steady-state waveforms and ZVS capability. Through a comprehensive ZVS analysis, an accurate approximation of the inductor current is proposed, addressing critical aspects of ZVS operation, including dynamic current behavior during dead time. The derived ZVS-currents, representing the minimum inductor current required for complete ZVS, establish precise ZVS constraints that minimize circulating currents while ensuring optimal ZVS performance. By integrating these precise ZVS calculations, the proposed TPS modulation scheme employs nonlinear optimization to minimize rms current and conduction losses. The method maximizes ZVS capability of the converter by increasing the number of switches achieving ZVS and expanding the all-ZVS operating region. Experimental results validate the effectiveness of the proposed scheme, demonstrating significant efficiency improvements over state-of-the-art approaches.

## References

[1] R. W. A. A. De Doncker, D. M. Divan, and M. H. Kheraluwala, "A three-phase soft-switched high-power-density DC/DC converter for high-power applications," *IEEE Trans. Ind. Appl.*, vol. 27, no. 1, pp. 63–73, Jan./Feb. 1991.

[2] F. Krismer and J. W. Kolar, "Accurate small-signal model for the digital control of an automotive bidirectional dual active bridge," *IEEE Trans. Power Electron.*, vol. 24, no. 12, pp. 2756–2768, Dec. 2009.

[3] H. Bai, C. Mi, C. Wang, and S. Gargies, "The dynamic model and hybrid phase-shift control of a dual-active-bridge converter," in *Proc. 34th Annu. Conf. IEEE Ind. Electron.*, Jan. 2008, pp. 2840–2845.

[4] D. Mou, Q. Luo, J. Li, Y. Wei, and P. Sun, "Five-degree-of-freedom modulation scheme for dual active bridge DC–DC converter," *IEEE Trans. Power Electron.*, vol. 36, no. 9, pp. 10584–10601, Sep. 2021.

[5] H. Wen, B. Su, and W. Xiao, "Design and performance evaluation of a bidirectional isolated DC–DC converter with extended dual-phase-shift scheme," *IET Power Electron.*, vol. 6, no. 5, pp. 914–924, 2013.

[6] J. Hu, S. Cui, D. v. d. Hoff, and R. W. De Doncker, "Generic dynamic phase-shift control for bidirectional dual-active bridge converters," *IEEE Trans. Power Electron.*, vol. 36, no. 6, pp. 6197–6202, Jun. 2021.

[7] B. Zhao, Q. Yu, and W. Sun, "Extended-phase-shift control of isolated bidirectional DC–DC converter for power distribution in microgrid," *IEEE Trans. Power Electron.*, vol. 27, no. 11, pp. 4667–4680, Nov. 2012.

[8] K. Wu, C. W. de Silva, and W. G. Dunford, "Stability analysis of isolated bidirectional dual active full-bridge DC–DC converter with triple phase-shift control," *IEEE Trans. Power Electron.*, vol. 27, no. 4, pp. 2007–2017, Apr. 2012.

[9] J. Yang et al., "Extension of zero-voltage switching region of wide volage ratio range dual-active-bridge converter by LC antiresonant network," *IEEE Trans. Emerg. Sel. Topics Power Electron.*, vol. 12, no. 1, pp. 172–185, Feb. 2024.

[10] D. Lyu, C. Straathof, T. B. Soeiro, Z. Qin, and P. Bauer, "ZVS-Optimized constant and variable switching frequency modulation schemes for dual active bridge converters," *IEEE Open J. Power Electron.*, vol. 4, pp. 801–816, 2023.
[11] M. Mahdavifard and S. A. Khajehoddin, "Closed-form continuous asymmetrical hybrid modulation, ensuring wide ZVS range and seamless transients for DAB converters," *IEEE Trans. Power Electron.*, vol. 39, no. 5, pp. 5776–5792, May 2024.
[12] S. Shao, H. Chen, X. Wu, J. Zhang, and K. Sheng, "Circulating current and ZVS-on of a dual active bridge DC-DC converter: A review," *IEEE Access*, vol. 7, pp. 50561–50572, 2019.
[13] G. G. Oggier, G. O. GarcÍa, and A. R. Oliva, "Switching control strategy to minimize dual active bridge converter losses," *IEEE Trans. Power Electron.*, vol. 24, no. 7, pp. 1826–1838, Jul. 2009.
[14] J. Everts, F. Krismer, J. Van den Keybus, J. Driesen, and J. W. Kolar, "Optimal ZVS modulation of single-phase single-stage bidirectional DAB AC–DC converters," *IEEE Trans. Power Electron.*, vol. 29, no. 8, pp. 3954–3970, Aug. 2014.
[15] S. Shao, M. Jiang, W. Ye, Y. Li, J. Zhang, and K. Sheng, "Optimal phase-shift control to minimize reactive power for a dual active bridge DC–DC converter," *IEEE Trans. Power Electron.*, vol. 34, no. 10, pp. 10193–10205, Oct. 2019.
[16] F. Krismer and J. W. Kolar, "Closed form solution for minimum conduction loss modulation of DAB converters," *IEEE Trans. Power Electron.*, vol. 27, no. 1, pp. 174–188, Jan. 2012.
[17] A. Tong, L. Hang, G. Li, X. Jiang, and S. Gao, "Modeling and analysis of a dual-active-bridge-isolated bidirectional DC/DC converter to minimize RMS current with whole operating range," *IEEE Trans. Power Electron.*, vol. 33, no. 6, pp. 5302–5316, Jun. 2018.
[18] G. Xu, D. Sha, J. Zhang, and X. Liao, "Unified boundary trapezoidal modulation control utilizing fixed duty cycle compensation and magnetizing current design for dual active bridge DC–DC converter," *IEEE Trans. Power Electron.*, vol. 32, no. 3, pp. 2243–2252, Mar. 2017.
[19] W. Choi, K.-M. Rho, and B.-H. Cho, "Fundamental duty modulation of dual-active-bridge converter for wide-range operation," *IEEE Trans. Power Electron.*, vol. 31, no. 6, pp. 4048–4064, Jun. 2016.
[20] Z. Guo, "Modulation scheme of dual active bridge converter for seamless transitions in multiworking modes compromising ZVS and conduction loss," *IEEE Trans. Ind. Electron.*, vol. 67, no. 9, pp. 7399–7409, Sep. 2020.
[21] L. Gong et al., "A dynamic ZVS-Guaranteed and seamless-mode-transition modulation scheme for the DAB converter that maximizes the ZVS range and lowers the inductor RMS current," *IEEE Trans. Power Electron.*, vol. 37, no. 11, pp. 13119–13134, Nov. 2022.
[22] N. Noroozi et al., "RMS current minimization in a SiC-based dual active bridge converter using triple-phase-shift modulation," *IEEE Trans. Ind. Electron.*, vol. 70, no. 7, pp. 7173–7182, Jul. 2023.
[23] J. Yang et al., "Online digital implementation of wide voltage range RMS-current-optimized control with voltage balancing capability for DAB converter," *IEEE Trans. Power Electron.*, vol. 38, no. 4, pp. 4360–4377, Apr. 2023.
[24] J. Huang, Y. Wang, Z. Li, and W. Lei, "Unified triple-phase-shift control to minimize current stress and achieve full soft-switching of isolated bidirectional DC–DC converter," *IEEE Trans. Ind. Electron.*, vol. 63, no. 7, pp. 4169–4179, Jul. 2016.
[25] J. Li, Q. Luo, D. Mou, Y. Wei, and X. Zhang, "Comprehensive optimization modulation scheme of low current level and wide ZVS range for dual active bridge converter with dead-zone control," *IEEE Trans. Power Electron.*, vol. 37, no. 3, pp. 2731–2748, Mar. 2022.
[26] X. Yang, J. Wang, Y. Du, C. Liu, T. Zhang, and J. Zhang, "Bidirectional ZVS operation of all switches for a DAB converter over a full range of loads with optimized current stress," *IEEE Trans. Ind. Appl.*, vol. 60, no. 1, pp. 1183–1195, Jan./Feb. 2024.
[27] N. Hou, W. Song, and M. Wu, "Minimum-current-stress scheme of dual active bridge DC–DC converter with unified phase-shift control," *IEEE Trans. Power Electron.*, vol. 31, no. 12, pp. 8552–8561, Dec. 2016.
[28] N. Li et al., "Single-degree-of-Freedom hybrid modulation strategy and light-load efficiency optimization for dual-active-bridge converter," *IEEE Trans. Emerg. Sel. Topics Power Electron.*, vol. 12, no. 4, pp. 3936–3947, Aug. 2024.
[29] Y. Yan, H. Bai, A. Foote, and W. Wang, "Securing full-power-range zero-voltage switching in both steady-state and transient operations for a dual-active-bridge-based bidirectional electric vehicle charger," *IEEE Trans. Power Electron.*, vol. 35, no. 7, pp. 7506–7519, Jul. 2020.
[30] L. Zhou, Y. Gao, H. Ma, and P. T. Krein, "Wide-load range multiobjective efficiency optimization produces closed-form control solutions for dual active bridge converter," *IEEE Trans. Power Electron.*, vol. 36, no. 8, pp. 8612–8616, Aug. 2021.
[31] R. W. Erickson and D. Maksimović, *Fundamentals of Power Electronics*. Cham: Springer, 2020.
[32] S. Dey and A. Mallik, "An online-optimized ZVS-current tracked soft-switching modulation for triple active bridge converter," *IEEE Trans. Power Electron.*, vol. 39, no. 11, pp. 14708–14728, Nov. 2024.
[33] A. K. Jain and R. Ayyanar, "PWM control of dual active bridge: Comprehensive analysis and experimental verification," *IEEE Trans. Power Electron.*, vol. 26, no. 4, pp. 1215–1227, Apr. 2011.

**Gayoung Park** (Graduate Student Member, IEEE) received the B.S. degree in electrical engineering, in 2023, from Seoul National University, Seoul, South Korea, where she is currently working toward the M.S. degree in electrical engineering.

Her research interests include isolated bidirectional dc–dc converter and control and optimization of power converters.

**Hwigon Kim** (Member, IEEE) received the B.S and Ph.D. degrees in electrical engineering from Seoul National University, Seoul, South Korea, in 2018 and 2023, respectively.

From 2023, he has been a Postdoctoral Researcher with Seoul National University Electric Power Research Institute, Seoul. His current research interests include control of power electronics and its application for electrical machines and dc–dc converters.

**Byung-Geuk Cho** was born in Busan, Korea, in 1980. He received the B.S., M.S., and Ph.D. degrees in electrical engineering from Seoul National University, Seoul, South Korea, in 2007, 2009, and 2015, respectively.

From 2015 to 2021, he worked with LS Electric Korea to develop general-purpose inverters for motor drives such as sensorless control and vector control. Since 2021, he has been working with LG Innotek Korea, Seoul. His current research interests include EV charging infrastructures and renewable energy.

**Shenghui Cui** (Member, IEEE) received the B.S. degree in electrical engineering from Tsinghua University, Beijing, China, in 2012, the M.S. degree in electrical engineering from Seoul National University, Seoul, South Korea, in 2014, and the Dr.-Ing. degree in electrical engineering with the highest distinction (summa cum laude) from RWTH Aachen University, Aachen, Germany, in 2019.

Since 2021, he has been an Assistant Professor with the Department of Electrical and Computer Engineering, Seoul National University. From 2015 to 2021, he has been with the Institute for Power Generation and Storage Systems, E.ON Energy Research Center, RWTH Aachen University, where he was a Research Associate and later on a Senior Scientist. His research interests include interaction of power systems and power converters, power converters in ac/dc utility applications, and applications of wide-band gap power devices.

Dr. Cui was the recipient of the STAWAG Best Dissertation Prize from Faculty of Electrical Engineering and Information Technology, RWTH Aachen University in 2019, the Second Place Prize Paper Award of the IEEE Transactions on Power Electronics in 2018, the Second Prize Paper Award of IEEE IPEC (ECCE Asia) in 2018, and the Outstanding Presentation Award of the IEEE Applied Power Electronics Conference in 2014.